Title
Capillary Leidenfrost effect

Journal
Nature Physics, 22(5)

ISSN
1745-2473

Authors
Zhang, Zhi
Zhang, Zhenwen
Ji, Bingqiang
et al.

Publication Date
2026-05-01

DOI
10.1038/s41567-026-03255-x

nature physics

Article

https://doi.org/10.1038/s41567-026-03255-x

Capillary Leidenfrost effect

Received: 14 September 2024

Accepted: 11 March 2026

Published online: 14 April 2026

Check for updates

Zhi Zhang [1,2,3,7], Zhenwen Zhang [1,2,3,7], Bingqiang Ji [1,2,7], Yongjiu Yuan[1,2,3,7], Wai Kin Lo [1,2], Xiong Wang[1,2], Xiaoxue Yao [1,2], Qili Xu[1,2], Chen Ling [1,2], Hyoungsoo Kim[4], Gang Kevin Li [5] ✉, Thomas Schutzius [6] ✉ & Steven Wang [1,2,3] ✉

The Leidenfrost effect, best known as the formation of an insulating vapour layer beneath a liquid droplet that delays boiling, offers great potential for droplet manipulation and drag reduction. However, regulating the conventional Leidenfrost effect remains challenging due to the complex liquid dynamics involved. Here we report a behaviour that we term the capillary Leidenfrost effect, which enables stable and sustained solid levitation driven by liquid evaporation. It occurs at a temperature threshold that is below the Leidenfrost point of its droplet counterpart, yet without the need for specialized surface manufacturing techniques. Our structure is composed of periodically arranged capillaries that stabilize the liquid interface, enhance heat conduction and provide liquid storage capacities. The capillary Leidenfrost effect is generic in widely accessible natural materials and metals. Our experiments demonstrate the feasibility of long-distance, sustained self-propulsion and load delivery on a practical scale. This mechanism facilitates potential applications from contactless transportation and drag reduction to extended-distance delivery in harsh environments.

The Leidenfrost effect[1] describes a liquid levitation state enabled by a continuous vapour layer when deposited on a sufficiently hot surface, deteriorating the heat transfer and extending the liquid lifetime. This effect is ubiquitous in a wide range of laboratory and industrial applications[2,3]. Previous studies[4–7] focused on suppressing the Leidenfrost effect by modifying surface characteristics, such as wettability and roughness. Meanwhile, the unique levitation state provided by the Leidenfrost effect presents a frictionless nature[8–10], offering enormous potential for liquid manipulations, with the manufacture of surface gradients in topography[11–16], wettability[17] and temperature[18,19]. However, the traditional Leidenfrost effect suffers from distinct dynamic behaviours[20–22] and oscillations[23] over the capillary length, making regulation and scaling up challenging, and the manipulations of the levitating droplet often depend on complex surface engineering techniques.

Here, we report a Leidenfrost behaviour termed the capillary Leidenfrost effect. This effect enables the stable levitation of a solid object on an untreated substrate through liquid evaporation within an integrated capillary structure (CS), representing a paradigm shift from droplet-based to solid-based Leidenfrost systems. This CS consists of periodically arranged capillaries that provide liquid absorption and storage capacities (Extended Data Fig. 1a,b). The liquid is infused onto the upper surface of CS and evaporates in capillaries through capillary action, resulting in the establishment of the Leidenfrost state within seconds (Fig. 1a and Supplementary Video 1). At the stable state, a vivid vapour film with a thickness of roughly 63 µm was observed by macrolens, as indicated by the gap between CS and its mirror reflection in the zoom-in view (Fig. 1a). This vapour film creates a nearly frictionless state, enabling CS to autonomously glide on the solid substrate without

[1]Department of Mechanical Engineering, City University of Hong Kong, Hong Kong, China. [2]Centre for Nature-inspiring Engineering, City University of Hong Kong, Hong Kong, China. [3]Hong Kong Institute for Clean Energy, City University of Hong Kong, Hong Kong, China. [4]Department of Mechanical Engineering, Korea Advanced Institute of Science and Technology, Daejeon, Republic of Korea. [5]Department of Chemical Engineering, The University of Melbourne, Melbourne, Victoria, Australia. [6]Department of Mechanical Engineering, University of California, Berkeley, Berkeley, CA, USA. [7]These authors contributed equally: Zhi Zhang, Zhenwen Zhang, Bingqiang Ji, Yongjiu Yuan. ✉e-mail: li.g@unimelb.edu.au; tschutzius@berkeley.edu; steven.wang@cityu.edu.hk

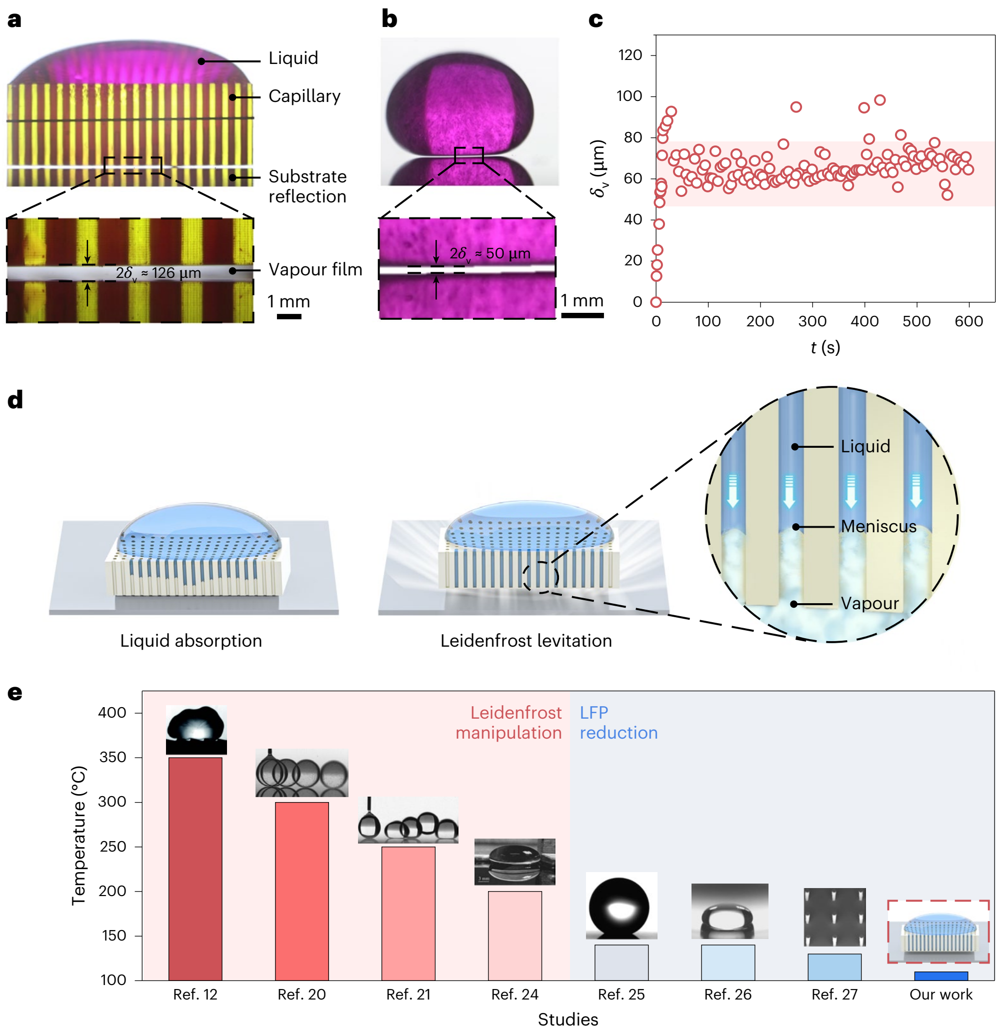

Fig. 1 | Capillary Leidenfrost effect. a, The Leidenfrost levitation state of CS. Copper wires are applied to restrain CS within the focal length, and the liquid is supplied from above to ensure the Leidenfrost effect is exclusively triggered by liquid evaporation in capillaries. The liquid medium used here is water. **b**, The Leidenfrost levitation state of the droplet. **c**, Variation of vapour film thickness when CS is subjected to impacts of water drops of 30 µl every 30 s. **d**, Schematic of the capillary Leidenfrost effect. **e**, Temperature comparison between our work and previous studies. Inset images in **e** are reproduced with permission from: ref. 12, Springer Nature Limited; ref. 20, Springer Nature Limited; ref. 21 under a Creative Commons license CC BY 4.0; ref. 24, AIP; ref. 25, American Chemical Society; ref. 26, APS; ref. 27, Springer Nature Limited.

any initial force (Extended Data Fig. 1c). This solid-based Leidenfrost effect mirrors the traditional droplet-based Leidenfrost effect (Fig. 1b), yet without the presence of a deformable liquid–vapour interface, allowing CS to levitate on its vapour film stably without suffering from the complex liquid dynamic behaviours. For example, a Leidenfrost droplet of comparable size to CS experiences violent, high-frequency, star-shaped oscillations. By contrast, CS maintains a stable Leidenfrost state throughout its lifespan, regardless of its size (Extended Data Fig. 2). This capillary Leidenfrost state could even be sustained for an extended period by intermittent liquid resupply. The vapour film thickness (δ_v) was measured to remain stable between 50 µm and 80 µm over a 10-min period when subjected to repeated liquid impacts of 30 µl every 30 s, demonstrating the excellent sustainability and stability of the capillary Leidenfrost effect (Fig. 1c).

Figure 1d schematically illustrates the physical process of the capillary Leidenfrost effect. When a droplet is placed on the upper surface of the CS, it rapidly permeates into the capillaries under the capillary effect and then evaporates. The resulting vapour escapes from the capillaries and subsequently forms a continuous film that effectively levitates the CS, as indicated in the magnified view. The fundamental distinction between the capillary Leidenfrost effect and the traditional droplet Leidenfrost effect is that droplet evaporation is replaced with capillary evaporation. This evaporation mechanism difference allows CS to achieve the Leidenfrost effect at a temperature threshold of only 110 °C, remarkably below the commonly recognized Leidenfrost point (LFP) of its liquid counterpart. As summarized in Fig. 1e, we compared the Leidenfrost temperatures from previous studies[12,20,21,24–27]. The red regime represents the temperature required for classic Leidenfrost dynamic behaviours, and the blue regime represents the LFP reduction achieved by conventional surface engineering techniques. Our work achieves an ultralow LFP without relying on specialized surface manufacturing techniques. This observation contrasts with existing studies[28], which suggested that the Leidenfrost effect requires a substrate temperature (T_{sub}) remarkably higher than the liquid's boiling point.

This dramatic difference in LFP is visually evident in Fig. 2a: a droplet and CS exhibit contrasting behaviours when in contact with the same substrate. The droplet experiences violent contact boiling and evaporates within 1.5 s, characterized by the formation and collapse of bubbles. By striking contrast, CS promptly achieves the Leidenfrost state after the liquid is pumped into the capillaries and maintains the levitation state for about 2 min (Supplementary video 2). The

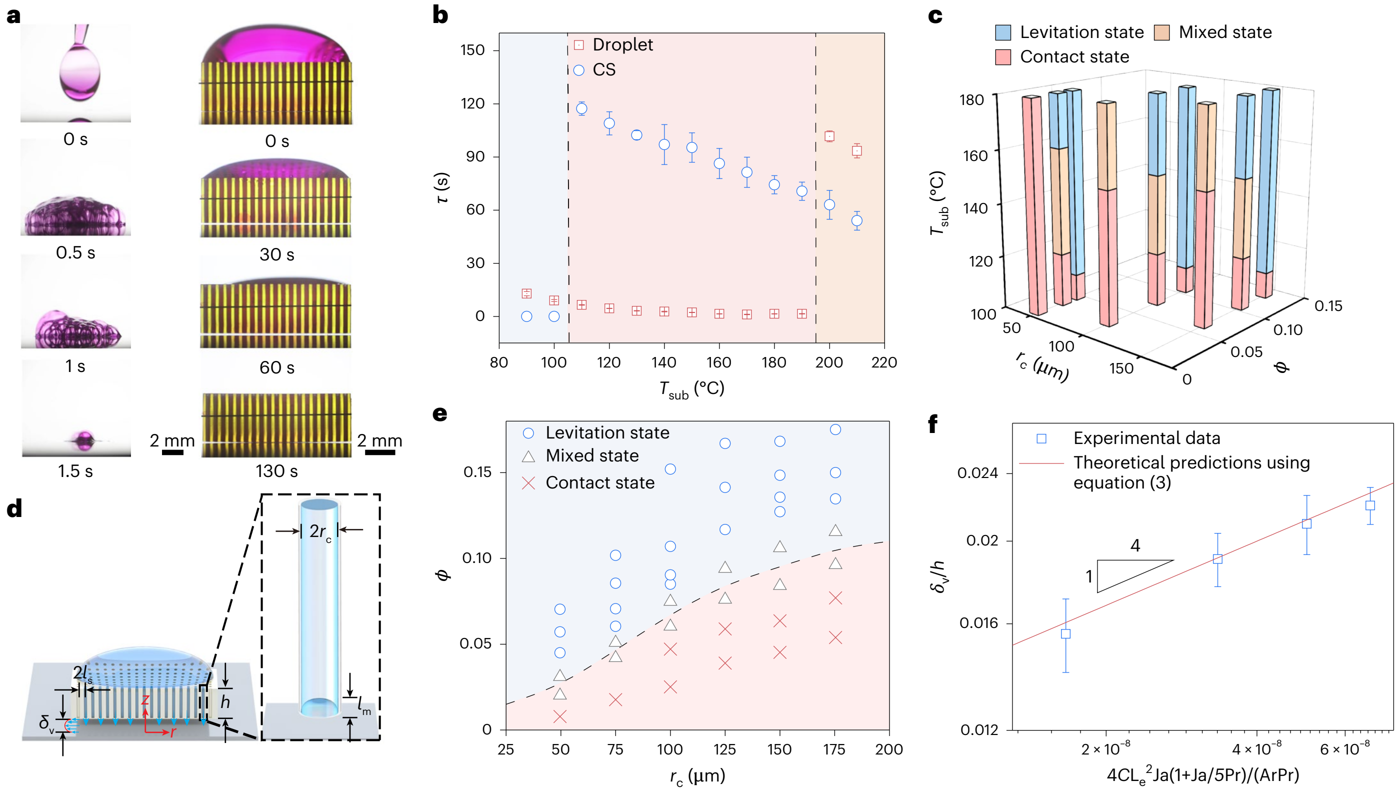

Fig. 2 | Capillary Leidenfrost characteristics and mechanism. **a**, Behaviour comparison between the droplet and wetted CS on the same substrate (silicon wafer) at 130 °C. **b**, Comparison of the droplet lifetime and CS levitation time at varying substrate temperatures. The droplet volume and the liquid volume applied to CS are both 80 µl. The radius r_c and porosity ϕ of CS are 150 µm and 0.24, respectively. The number of testing samples was $n = 3$, and data are presented as mean values ± s.e.m. The colours in the background highlight the Leidenfrost transitions of CS and the droplet. **c**, Influence of capillary radius and porosity on CS states at different substrate temperatures. **d**, Schematic of a CS levitating on its own vapour film. The magnified view reveals the liquid evaporation in a single capillary tube. **e**, Phase map for the capillary Leidenfrost effect. **f**, Comparison of normalized vapour film thickness between experimental measurements and theoretical predictions. The number of testing samples was $n = 5$, and data are presented as mean values ± s.e.m. $C = 0.694$; $Ar = 1.466 \times 10^6$; $L_e = 1.33$; $Pr = 1.87$.

temperature evolution is observed by infrared cameras, demonstrating a steady increase along the vertical direction (Extended Data Fig. 3a). We further compared the lifetime of a droplet and levitation time of CS at different substrate temperatures (Fig. 2b). The droplet lifetime initially decreases slightly, and then abruptly jumps at approximately 200 °C, indicating the transition to the Leidenfrost state. By contrast, the CS initiates the levitation state once the T_{sub} exceeds the boiling point of 100 °C. A sequence of infrared images demonstrates that a CS deposited on a hot surface of 110 °C initially remains stationary, then self-propels frictionlessly after a few seconds of heating, indicating the generation of a lubrication vapour film beneath it (Extended Data Fig. 3b). This ultralow LFP could remarkably reduce the critical heat flux needed to initiate the Leidenfrost effect, by a factor of 5.6 compared with a typical metallic surface.

Moreover, the LFP is shown to be tunable across a wide range of structural parameters, specifically the capillary radius (r_c) and porosity (ϕ). It is observed that CSs with different structural parameters exhibit distinct states with increasing T_{sub}, including contact state, mixed state and levitation state (Fig. 2c and Extended Data Fig. 4). The mixed state represents a transition phase characterized by incomplete levitation, where insufficient vapour flux leads to localized solid–liquid contact and intermittent oscillations. The LFP, ranging from 110 °C to 160 °C, is found to decrease with increasing ϕ and decreasing r_c. Specifically, a smaller capillary radius facilitates liquid evaporation, while a larger porosity enhances the liquid retention capacity, synergistically boosting the levitation force and contributing to the occurrence of the Leidenfrost effect at lower T_{sub}. This discovery suggests that the LFP of CS can be effectively controlled by altering r_c and ϕ, thereby offering a practical solution for the temperature-regulated Leidenfrost effect without requiring complex surface engineering.

For a specific T_{sub}, we quantitatively examined the critical conditions for the onset of the capillary Leidenfrost effect. The resultant phase map (Fig. 2e) indicates that the capillary Leidenfrost state is favoured by a small capillary radius and a large porosity, with a clear boundary delineated by the mixed states. The critical porosity, the threshold for levitation, varies from approximately 0.025 to 0.1 across the range of capillary radii tested. Notably, CS with such low porosity can generate a sufficient levitation force to counteract gravity. This finding provides direct validation of the remarkable evaporation enhancement induced by capillary confinement. Furthermore, with the increase in substrate temperature, the critical porosity could be reduced even further. This analysis offers a fundamental framework for the future design of CS to initiate and sustain the capillary Leidenfrost effect.

The capillary Leidenfrost effect is also influenced by the properties of the liquid medium. For example, we examined the response of CS when subjected to the impacts of ethanol drops. It was observed that ethanol cannot be retained in the capillaries owing to its low surface tension and the good wettability of the capillaries by the ethanol. Consequently, it directly contacts the substrate, resulting in violent vibration of CS (Extended Data Fig. 5). Therefore, to achieve a stable Leidenfrost state at low T_{sub}, the liquid should be carefully selected to favour the liquid retention within capillaries.

We then explore the underlying physics governing the capillary Leidenfrost effect through theoretical modelling. At a quasi-steady state, the levitation of an object on a vapour film is governed by the balance between viscous pressure and gravitational stress. We begin with the classical theoretical framework for the Leidenfrost droplet developed by Arpaci et al.[29], which provides a fundamental derivation for the vapour film thickness, δ_v (Supplementary Discussion):

$$\delta_v = \left[\frac{4\mu_v a \mathrm{Ja} R^2}{(\rho_l - \rho_v) g h}\left(1 + \frac{\mathrm{Ja}}{5\,\mathrm{Pr}}\right)\right]^{\frac{1}{4}}, \quad (1)$$

where $a = \frac{k_v}{\rho_v c_p}$ is the thermal diffusivity of the vapour, k_v is the thermal conductivity of vapour, ρ_v is the vapour density, c_p is the specific heat capacity of the vapour, $\mathrm{Ja} = \frac{c_p(T_{sub} - T_s)}{L}$ is the Jakob number, T_{sub} is the substrate temperature, T_s is the temperature at the liquid–vapour interface, which is essentially the saturation temperature, L is the latent heat, $\mathrm{Pr} = \frac{\mu_v c_p}{k_v}$ is the vapour Prandtl number, μ_v is the vapour viscosity, g is the gravitational acceleration, R and h are the droplet radius and height, and ρ_l is the liquid density.

While equation (1) successfully predicts the vapour film thickness for a droplet, its application to the CS requires a critical modification. The fundamental difference lies in the heat transfer pathway from the substrate to the evaporating interface. For a Leidenfrost droplet, heat conducts uniformly from the substrate through a continuous vapour film to the droplet. By contrast, the base of CS is partitioned into pores and solid pillars, creating two distinct and parallel paths for heat to reach the meniscus (Extended Data Fig. 6).

(1) Pore area path: heat directly conducts through the vapour film to the meniscus (analogous to the droplet case). The heat resistance (R_I) is expressed as: $R_I = R_{v(pore)} = \frac{\delta_v}{k_v \phi A}$, where $R_{v(pore)}$ is the resistance of the vapour film at pore area, ϕ is the porosity, and A is the bottom surface area of CS.

(2) Solid area path: heat first conducts through the vapour film to the solid, then laterally through the solid to the liquid film in the meniscus, and finally to the interface. The heat resistance of the liquid film ($R_l \approx 0$) is negligible due to the extremely thin liquid film ($\delta_l \approx 10$–100 nm) at the evaporating thin-film region of the meniscus.

Hence, the total heat resistance (R_{II}) is expressed as $R_{II} = R_{v(solid)} + R_s = \frac{\delta_v}{k_v(1-\phi)A} + \frac{l_s}{k_s n A_m}$, where $R_{v(solid)}$ is the heat resistance of vapour film at the solid area, R_s is the heat resistance across the solid, k_s is the thermal conductivity of the solid, l_s is the characteristic length, which represents the half of the distance between two adjacent capillary walls, A_m is the effective heat transfer area for a single meniscus, which is the lateral surface area of the meniscus-coated pore wall, $A_m = 2\pi r_c l_m$, where l_m is the axial length of the meniscus region along the capillary wall (Fig. 2d), and n is the number of capillaries. To simplify the expression, $R_{II} = R_{v(solid)} + R_s$, a dimensionless coefficient (K) is introduced to quantify the relative importance of heat resistance across the solid to that across the vapour film, $K = \frac{R_s}{R_{v(solid)}}$. This allows us to reduce the expression as $R_{II} = (1+K)R_{v(solid)}$.

Then, the heat equation is modified as

$$\dot{m}L = \phi A \frac{k_v}{\delta_v}\Delta T + (1-\phi)A\frac{k_v}{(1+K)\delta_v}\Delta T, \quad (2)$$

where $\dot{m}$ is the evaporating mass flux, and $\Delta T = T_{sub} - T_s$. A unified heat transfer coefficient C is introduced, $C = \phi + \frac{(1-\phi)}{(1+K)}$. Equation (2) is hence reduced to $\dot{m}L = CA\frac{k_v}{\delta_v}\Delta T$. The coefficient C embodies the efficiency of heat utilization. When $K \to 0$, $C \to 1$, this represents the case of highly conductive solids, where heat conducted through the solid area is effectively used for evaporation. Conversely, when $K \to \infty$, $C \to \phi$, this represents the case of poorly thermally conductive solids, where heat transferred to the solid is largely dissipated, making only the pore-area path effective. Under our experimental conditions, K is calculated in the range from 0.86 to 0.49, indicating the experiments are close to the highly conductive solid regime. We take the average value $K = 0.675$ for subsequent calculations.

Substituting the modified heat equation into the Arpaci model yields the new vapour film thickness expression for the CS, $\delta_v = [\frac{4C\mu_v a \mathrm{Ja} R^2}{(\bar{\rho}-\rho_v)gh}(1 + \frac{\mathrm{Ja}}{5\,\mathrm{Pr}})]^{\frac{1}{4}}$, where $\bar{\rho}$ is the average density of CS and liquid. We here define a geometry aspect ratio, $L_e = \frac{R}{h}$, where h is the CS height, and normalize the δ_v by the h, yielding

$$\frac{\delta_v}{h} = \left[4C\frac{{L_e}^2}{\mathrm{Ar}}\frac{\mathrm{Ja}}{\mathrm{Pr}}\left(1 + \frac{\mathrm{Ja}}{5\,\mathrm{Pr}}\right)\right]^{\frac{1}{4}}, \quad (3)$$

where $\mathrm{Ar} = \frac{(\bar{\rho}-\rho_v)\rho_v g h^3}{{\mu_v}^2}$ is Archimedes number. In equation (3), $\frac{{L_e}^2}{\mathrm{Ar}}$ describes the effects of CS geometry and gravity on vapour film thickness. $\frac{\mathrm{Ja}}{\mathrm{Pr}}$ embodies the dynamic competition between the rate of vapour generation and the resistance of vapour escape, synergically determining the vapour film thickness. $1 + \frac{\mathrm{Ja}}{5\,\mathrm{Pr}}$ is a factor that ranges from 1.004 to 1.015 under our experimental conditions. By assuming $1 + \frac{\mathrm{Ja}}{5\,\mathrm{Pr}} = 1$, the scaling law of $\delta_v \propto \Delta T^{\frac{1}{4}}$ is derived through the Ja number, which arises from the coupling between the Poiseuille flow in the vapour film (where vapour pressure $p \propto {\delta_v}^3$) and heat conduction to the interface (where evaporation rate $\dot{m} \propto \frac{1}{\delta_v}$). Substituting all known parameters from Supplementary Table 1 into equation (3), the theoretical relationship was plotted on a double-logarithmic figure, showing excellent agreement with the experimental data (Fig. 2f). This close correspondence strongly validates the accuracy of our theoretical model.

The Leidenfrost effect, characterized by negligible friction between the levitating object and the substrate, typically requires engineered surface gradients for directional droplet motion on the substrate. By contrast, our CS could achieve directional motion simply through the design of tilted capillaries, without the need for a gradient surface (Fig. 3a). The magnified view illustrates the liquid evaporation within tilted capillaries, enabling an asymmetric vapour escape and the formation of a wedged vapour film.

To systematically investigate the role of the capillary tilted angle (β) on self-propulsion, we fabricated a series of CSs with β ranging from 0° to 30° and characterized their motion on a heated substrate. When released from an identical starting position, CSs with different β values exhibited notably different travel distances over 1.5 s (Fig. 3b and Supplementary Video 3). The magnified view confirmed the presence of a wedged vapour film with a characteristic tilted angle (φ) of 0.33°. The travel distance (s) follows a parabolic relationship with time, indicating uniformly accelerated motion (Extended Data Fig. 7a). The propulsion performance was optimized at β = 15–20°, where CSs achieved peak speeds of approximately 53 ± 5 mm s^{-1} (Fig. 3c). High-speed imaging reveals three distinct vapour film morphologies as a function of inclination angle, including uniform vapour film, wedged vapour film and incomplete vapour film. Specifically, the moderate increase of β (0–20°) creates an asymmetric vapour escape, providing a horizontal propulsive force. However, further increase of β (20–30°) results in a more asymmetric mass distribution of CS, hindering levitation on the heavier side due to insufficient local vapour generation. Besides, the shape asymmetry becomes more pronounced with increasing tilted angle, making it more vulnerable to thermal stress. To alleviate thermal deformation, our experiments are limited to a substrate temperature of only 150 °C. Subsequent experiments confirmed that increasing the T_{sub} facilitates self-propulsion (Extended Data Fig. 7b), because the enhanced evaporation generates a thicker vapour layer, enabling a larger horizontal driven force.

A comprehensive force analysis was performed on the CS levitating above the wedged vapour film (Fig. 3a). The asymmetric design of

 https://doi.org/10.1038/s41567-026-03255-x

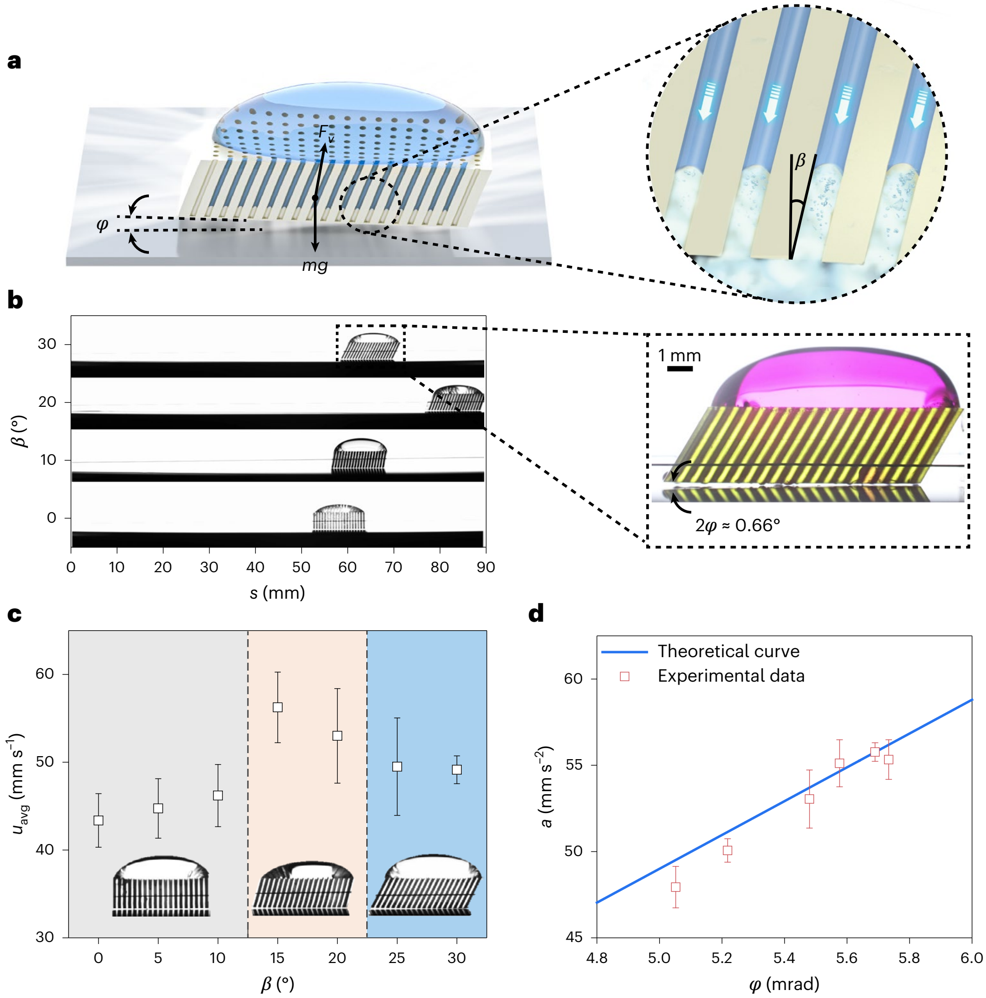

Fig. 3 | CS directional movement. **a**, Force analysis of CS with tilted capillaries levitating on a heated surface. The magnified view reveals the liquid evaporation in the tilted capillaries. **b**, A sequence of high-speed images capturing the travel distance of CS with different tilted angles within 1.5 s. A tiny tilting angle (≈0.25°) is prescribed on the substrate to ensure unidirectional movements, in case CS with small β cannot provide sufficient propulsive force against surface unevenness. The zoom-in view reveals the presence of a wedged vapour film. **c**, The average speed (u_{avg}) of CS with varying β. Insets: three distinct levitation states. The number of testing samples was $n = 3$, and data are presented as mean values ± s.e.m. **d**, Comparison of CS accelerations between experimental data and theoretical curve.

the tilted capillaries produces a horizontal component in the levitation pressure force, which acts as the propulsive mechanism for the CS. This propulsive mechanism can be modelled by analogy to an object sliding on a slope with a tilted angle of φ, which is equivalent to the tilted angle of the wedged vapour film[18,20]. The propulsive force (F_p) corresponds to the horizontal component of levitation force F_v, which can be expressed as: $F_p = F_v \sin \varphi$. At the steady state, $F_v = mg$, the acceleration (a) could be derived as

$$a = g \sin \varphi. \quad (4)$$

Given the minimal vapour film angle, the small angle approximation, $\sin \varphi \approx \varphi$ holds. Substituting this into equation (4) yields a linear relationship, $a = g\varphi$. By comparing with the measured accelerations at different tilting angles, our theoretical model aligns closely with experimental data, supporting the validity and accuracy of our hypothesis (Fig. 3d).

We further integrated the tilted capillary design into a racing car prototype, and observed its successful running through a winding horizontal track (Extended Data Fig. 8a), demonstrating the practical utility of the new tilted CS design in achieving directional movement. To address the thermal deformation issue encountered by three-dimensionally (3D)-printed resin, we also used a femtosecond laser technique for drilling microchannels in a metal cuboid, creating periodically spaced capillary channels. The machined metal CS allows the operation at remarkably higher substrate temperatures than the 3D-printed counterpart, thereby offering a faster evaporation rate and a larger levitation force. This feature enables the metal CS to achieve a stable Leidenfrost levitation and frictionless motion with a porosity of only 0.028, remarkably lower than the critical porosity of the printed CS ($\phi_c = 0.095$), despite its much higher density in comparison (Extended Data Fig. 8b). This metallic CS provides a practical solution for harnessing the capillary Leidenfrost effect under high-temperature conditions.

Finally, we discuss how the capillary Leidenfrost effect can be generalized to natural materials. We aim to explore economical and readily available natural materials as alternatives to the 3D-printed CS and metallic CS, which both require substantial investments and lengthy manufacturing periods. Through numerous tests, it has been proven that natural materials with high porosity and low density, such as balsa wood and cuttlebone, are optimal candidates for achieving a stable Leidenfrost state comparable to the engineered CS.

Balsa wood, recognized as one of the lightest hardwoods, exhibits a density typically ranging from 60 to 300 kg m^{-3} and a porosity

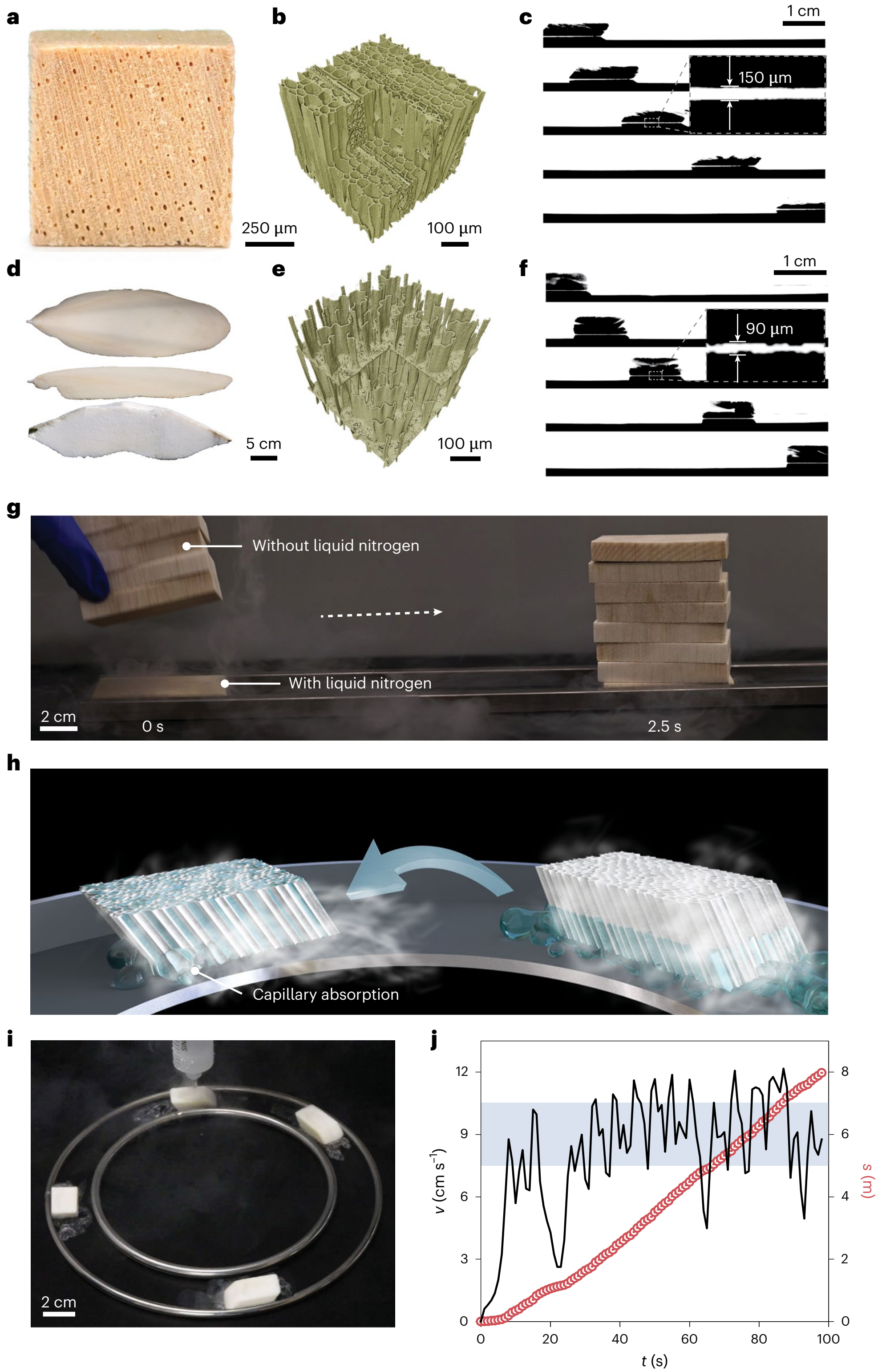

Fig. 4 | Sustained and long-distance self-propulsion. **a**, Digital image of balsa wood. **b**, A 3D micro-CT scanning image of balsa wood. **c**, A sequence of high-speed images capturing the frictionless movement of balsa wood on a gas film of about 75 µm. The time interval between two consecutive images is 300 ms. **d**, Digital images show the cuttlebone from different views. **e**, A 3D micro-CT scanning image of cuttlebone. **f**, A sequence of high-speed images capturing the frictionless movement of cuttlebone on a gas film of about 45 µm. The time interval between two consecutive images is 300 ms. The thinner gas film compared with balsa wood is induced by a heavier weight. **g**, Demonstration of the load delivery capacity of balsa wood at Leidenfrost levitation state. **h**, Schematic for automatic liquid resupply mechanism by capillary effect. **i**, A sequence of digital images showing the set-up and cuttlebone self-propulsion on a circular track. The time interval between two consecutive frames is 1.5 s. **j**, The speed and travel distance of cuttlebone self-propulsion against time. Cuttlebone accelerates rapidly and then runs for about 8 m in 100 s with an average speed of roughly 9 cm s^{-1}.

reaching up to 90% (Fig. 4a). It consists of three types of cell: compactly distributed tracheids (20–50 μm) and scattered large vessel channels (150–370 μm) that collectively function as interconnected pathways for liquid absorption and transportation along the growth direction, and ray cells that separate them in banded shape (Extended Data Fig. 9a). The internal 3D architecture, revealed by micro-computed tomography (micro-CT) scanning, demonstrates a compact capillary design structurally analogous to the engineered CS (Fig. 4b). The cuttlebone, shaped like an ellipse, is located at the dorsal side of the cuttlefish (Fig. 4d). It consists of numerous walls and septa that collectively separate the cuttlebone into numerous chambers. The typical wall height and chamber width are about 200–400 μm and 50–150 μm, respectively (Extended Data Fig. 9b). The intricate 3D structure, also visualized through micro-CT scanning, reveals a multitiered design (Fig. 4e). We immersed the balsa wood and cuttlebone samples in liquid nitrogen and then deposited on the same substrate and observed the self-propulsion without any external forces, the gas film is measured at approximately 75 μm and 45 μm, proving the establishment of the Leidenfrost levitation state (Fig. 4c,f and Supplementary Video 4). Notably, by replacing water with liquid nitrogen, we successfully reproduced the capillary Leidenfrost effect at room temperature, without the need for a heated surface.

To scale up the capillary Leidenfrost effect to a practical scale, we conducted long-distance motion tests of cuttlebone and balsa wood on an optical table. Remarkably, both materials demonstrate the ability to self-propel along a straight track for over 1 m without the need for initial force (Supplementary Video 4). To test the load capabilities of the capillary Leidenfrost effect, we deposited seven additional wood plates on a balsa wood plate that was immersed in liquid nitrogen. It was observed that one balsa wood plate can levitate seven additional wood plates and self-propel for over half a metre (Fig. 4g and Supplementary Video 5), suggesting its potential for load delivery. However, the liquid depletes quickly when levitating a heavy weight, prompting our interest in sustaining the Leidenfrost state by liquid resupply during motion. We hence designed a circular track with a needle syringe functioning as a 'liquid station' (Fig. 4i). A cuttlebone featuring a tilted capillaries design not only acquires the liquid directly from the 'liquid station', but also automatically collects the scattered liquid on the track through capillary action, thereby providing sustained liquid nitogen source for sustained self-propulsion (Fig. 4h and Supplementary Video 5). Impressively, the cuttlebone runs for about 8 m in 100 s with an average speed of roughly 9 cm s^{-1}. Even after 100 s, the cuttlebone's speed exhibits no signs of decline, providing strong evidence for the effectiveness of this design (Fig. 4j). These observations highlight the enormous potential of the capillary Leidenfrost effect in realizing long-distance and sustained self-propulsion on a practical scale. Although the capillary Leidenfrost effect on natural materials cannot be regulated by modifying structure parameters such as 3D-printing structures, their cost-effectiveness, widespread availability and substantial size render them ideal candidates for future practical applications.

In conclusion, this study reports a solid Leidenfrost behaviour occurring at a temperature threshold notably lower than the commonly acknowledged LFP of a droplet. We have elucidated the underlying physical mechanism by establishing robust relations among the governing non-dimensional numbers. Our study further demonstrated that this capillary Leidenfrost effect could potentially be used for directional motion without surface gradients. This effect is remarkably generic and applicable not only to 3D-printed materials, but also natural materials, and even metals, showcasing substantial promise for harnessing this effect in sustained and long-distance self-propulsion on a practical scale. From a broader perspective, this study opens a new avenue for exploring the Leidenfrost effect in solid-based systems, representing an important advancement over the conventional Leidenfrost droplet studies.

Online content

Any methods, additional references, Nature Portfolio reporting summaries, source data, extended data, supplementary information, acknowledgements, peer review information; details of author contributions and competing interests; and statements of data and code availability are available at https://doi.org/10.1038/s41567-026-03255-x.

References

1. Leidenfrost, J. G. & Aquae, D. *Communis Nonnullis Qualitatibus Tractatus* (Ovenius, 1756).
2. Dhillon, N. S., Buongiorno, J. & Varanasi, K. K. Critical heat flux maxima during boiling crisis on textured surfaces. *Nat. Commun.* **6**, 8247 (2015).
3. Tran, T., Staat, H. J., Prosperetti, A., Sun, C. & Lohse, D. Drop impact on superheated surfaces. *Phys. Rev. Lett.* **108**, 036101 (2012).
4. Kwon, H., Bird, J. C. & Varanasi, K. K. Increasing Leidenfrost point using micro-nano hierarchical surface structures. *Appl. Phys. Lett.* **103**, 201601 (2013).
5. Jiang, M. et al. Inhibiting the Leidenfrost effect above 1,000 degrees C for sustained thermal cooling. *Nature* **601**, 568–572 (2022).
6. Farokhnia, N., Sajadi, S. M., Irajizad, P. & Ghasemi, H. Decoupled hierarchical structures for suppression of Leidenfrost phenomenon. *Langmuir* **33**, 2541–2550 (2017).
7. Wakata, Y. et al. How roughness and thermal properties of a solid substrate determine the Leidenfrost temperature: experiments and a model. *Phys. Rev. Fluids* **8**, L061601 (2023).
8. Vakarelski, I. U., Patankar, N. A., Marston, J. O., Chan, D. Y. & Thoroddsen, S. T. Stabilization of Leidenfrost vapour layer by textured superhydrophobic surfaces. *Nature* **489**, 274–277 (2012).
9. Vakarelski, I. U., Marston, J. O., Chan, D. Y. & Thoroddsen, S. T. Drag reduction by Leidenfrost vapor layers. *Phys. Rev. Lett.* **106**, 214501 (2011).
10. Saranadhi, D. et al. Sustained drag reduction in a turbulent flow using alow-temperature Leidenfrost surface. *Sci. Adv.* **2**, e1600686 (2016).
11. Linke, H. et al. Self-propelled Leidenfrost droplets. *Phys. Rev. Lett.* **96**, 154502 (2006).
12. Lagubeau, G., Le Merrer, M., Clanet, C. & Quéré, D. Leidenfrost on a ratchet. *Nat. Phys.* **7**, 395–398 (2011).
13. Li, J. et al. Directional transport of high-temperature Janus droplets mediated by structural topography. *Nat. Phys.* **12**, 606–612 (2016).
14. Liu, M. et al. Inhibiting random droplet motion on hot surfaces by engineering symmetry-breaking Janus-mushroom structure. *Adv. Mater.* **32**, e1907999 (2020).
15. Li, A. et al. Tailoring vapor film beneath a Leidenfrost drop. *Nat. Commun.* **14**, 2646 (2023).
16. Bormashenko, E. Motion of the liquid on the surface of Leidenfrost droplets and the hairy ball theorem. *Surf. Innov.* **7**, 101–103 (2019).
17. Chen, M., Jia, Z., Zhang, T. & Fei, Y. Self-propulsion of Leidenfrost droplets on micropillared hot surfaces with gradient wettability. *Appl. Surf. Sci.* **433**, 336–340 (2018).
18. Bouillant, A., Lafoux, B., Clanet, C. & Quéré, D. Thermophobic Leidenfrost. *Soft Matter* **17**, 8805–8809 (2021).
19. Lin, Y., Wu, X., Hu, Z. & Chu, F. Leidenfrost droplet jet engine by bubble ejection. *J. Colloid Interface Sci.* **650**, 112–120 (2023).
20. Bouillant, A. et al. Leidenfrost wheels. *Nat. Phys.* **14**, 1188–1192 (2018).
21. Graeber, G. et al. Leidenfrost droplet trampolining. *Nat. Commun.* **12**, 1727 (2021).
22. Lyu, S. et al. Final fate of a Leidenfrost droplet: explosion or takeoff. *Sci. Adv.* **5**, eaav8081 (2019).

23. Bouillant, A., Cohen, C., Clanet, C. & Quéré, D. Self-excitation of Leidenfrost drops and consequences on their stability. *Proc. Natl Acad. Sci. USA* **118**, e2021691118 (2021).
24. Biance, A. L., Clanet, C. & Quéré, D. Leidenfrost drops. *Phys. Fluids* **15**, 1632–1637 (2003).
25. del Cerro, D. A. et al. Leidenfrost point reduction on micropatterned metallic surfaces. *Langmuir* **28**, 15106–15110 (2012).
26. Harvey, D., Harper, J. M. & Burton, J. C. Minimum Leidenfrost temperature on smooth surfaces. *Phys. Rev. Lett.* **127**, 104501 (2021).
27. Huang, W. et al. Low-temperature Leidenfrost-like jumping of sessile droplets on microstructured surfaces. *Nat. Phys.* **20**, 1274–1281 (2024).
28. Quéré, D. Leidenfrost dynamics. *Annu. Rev. Fluid Mech.* **45**, 197–215 (2013).
29. Arpaci, V. S. & Larsen, P. S. *Convection Heat Transfer* (Prentice Hall, 1984).

Methods

Natural materials

Balsa wood and cuttlebone were purchased online and manually sectioned using a stainless-steel blade. To soften the balsa wood for easier cutting, it was immersed in boiling water for approximately 30 min and subsequently dried in an incubator. The cuttlebone was carefully polished after sectioning and then cleaned using a dust-blowing ball.

Scanning electron microscopy

Cuttlebone and balsa wood were air-dried and then coated with an approximately 1.6-nm-thick gold layer by a Q150T plus sputter coater. Then, the samples were imaged with a field-emission scanning electron microscope (QUANTA FEG 450) with an accelerating voltage of 30.0 kV and a working distance of ~12.4 mm.

3D micro-CT scanning

The interior microstructures of cuttlebone and balsa wood were scanned using X-ray micro-CT with a nanoVoxel-3000 system. The scans were performed at a 1-µm voxel resolution with an exposure time of 0.25 s per projection, using an operating voltage of 60 kV and a current of 60 µA. Each sample underwent a 2-h scanning procedure, acquiring 1,800 frames per scan for comprehensive structural characterization.

3D printing

A series of CSs was fabricated using a nanoArch S140 3d printer (BMF Precision Tech). The printing material is a high-temperature resistant resin (HT200) that was developed by BMF Nano Materials Technology, with a tensile strength of 88 MPa and an elastic modulus of 3.1 GPa, respectively. The 3D model was constructed using a computer-aided design application and then converted into black-and-white planar slices using slicing software (Magics print for BMF 23.2). The CS was printed layer by layer under 405-nm ultraviolet light, with energy density, exposure time, resolution and layer thickness being 30 mW cm^{-2}, 1 s, 10 µm and 10 µm, respectively.

After printing, the CS was subjected to a thorough ethanol rinsing and then dried naturally at room temperature. Then, the printed CSs were subjected to a stepwise heat treatment in a vacuum drying oven (DZF-6020) as follows: heated to 120 °C and held for 30 min; increased to 150 °C in 60 min and then maintained for 120 min; gradually cooled to 140 °C in 30 min, cooled to 125 °C in 30 min and then cooled to 50 °C in 30 min; power-off and natural cooling to room temperature. This thermal protocol ensured optimal heat resistance while preserving structural integrity. Finally, capillary dimensions were measured using optical microscopy to evaluate the printing accuracy.

CS size effect test

A series of experiments was conducted using CSs with different sizes to evaluate their performance. Experimental results illustrated that both length (l) and width (w) exhibited a negligible effect on the capillary Leidenfrost effect (Extended Data Fig. 2c), whereas CS height (h) is proportional to the weight per unit area, thus requiring a careful optimization to favour the counterbalance of gravitational force. Within our experimental temperature range (100–200 °C), we determined that maintaining CS height below 5 mm was critical for sustaining a stable Leidenfrost state. Based on these findings, all subsequent experiments used standardized CS dimensions of l = 10 mm, w = 5 mm and h = 3 mm.

High-speed imaging

A high-speed camera (pc0.dimax HS4) equipped with a zoomed lens was used to record time-series images of the capillary Leidenfrost effect. A zoom lens (AF Micro-Nikkor 60 mm f/2.8 D) was attached to a high-speed camera to capture enlarged images. A continuous light plate (model: XCY-APC-04-2H-24) was deposited to increase the light flux to the camera and, hence, reduce noise in the images. The images were recorded at 1-ms intervals (1,000 fps), and the resolution of the image was 2,000 × 2,000 pixels.

Characterization of morphology

The macroscopic structures of balsa wood, cuttlebone and CS were observed by a digital mirrorless camera (Canon EOS R5) with an EF 100 mm f/2.8 L macrolens. For higher-resolution imaging of vapour film dynamics, we used an Optem FUSION Lens (OPTEM S/N 18F0090) to achieve micrometre-scale magnification.

Thermal conductivity measurement

The tested sample was a 20 × 20 × 4 mm cuboid, and the thermal conductivity was measured by TPS 2500S under an experimental temperature range. The instrument uses a double-spiral nickel alloy sensor that serves as both a heat source and a temperature sensor. A constant power current is passed through the probe to record the temperature changes over time. These temperature-versus-time data are then analysed to determine the thermal conductivity of the material in contact with the sensor.

Experimental set-up

The experimental set-up comprised four primary components (Extended Data Fig. 10a): (1) a temperature-controlled hot plate, (2) a high-speed camera (pco.dimax HS4) with synchronized illumination, (3) an infrared high-speed camera and (4) a K-type thermocouple for temperature measurement. Untreated silicon wafers served as substrates throughout the experiments. We infused distilled water onto the upper surface of the CS with a pipette instead of immersing the CS in a liquid container. This approach was specifically designed to ensure that the Leidenfrost levitation state is induced solely by liquid evaporation within the capillaries, thereby eliminating the liquid membrane that adheres to the structure surface by immersion. To facilitate our observation, copper wires function as a straight track that restrains CS within the focal plane, preventing frictionless movement induced by the Leidenfrost state. The establishment of the capillary Leidenfrost effect was recorded by a high-speed camera (pc0.dimax HS4) and an infrared high-speed camera (FLIR A6573 MWIR) operating at 120 Hz. The emissivity was set at 0.95 for CS. The vapour layer thickness (δ_v) and vapour tilting angle (φ) were measured through frame-by-frame image processing using ImageJ software.

Femtosecond laser processing

The femtosecond laser processing set-up is illustrated in Extended Data Fig. 10b. We used a Ti:sapphire laser regenerative amplifier system, which emitted the Gaussian beam with a central wavelength of 800 nm and a pulse duration of 35 fs. Before processing, the aluminium cuboid was ultrasonically cleaned in ethanol and then deposited on a computer-controlled X–Y workbench. The manufacturing process was conducted in ambient air, and the drilling diameter was 300 µm.

Data availability

All data are available in the Article or its Supplementary Information. Source data are provided with this paper.

Acknowledgements

This work was supported by the Research Grants Council of Hong Kong (grant no. 11217523). We appreciate the valuable and insightful comments on the theoretical aspects provided by D. Quéré. We acknowledge the initial strong support from G. McKinley and D. Poulikakos when we started this work almost 10 years ago.

Author contributions

Conceptualization: S.W., G.K.L., Zhi Zhang and T.S. Methodology: Zhi Zhang, Zhenwen Zhang, B.J. and Y.Y. Investigation: Zhi Zhang, Zhenwen Zhang, B.J., Y.Y., W.K.L., X.W., X.Y., C.L., Q.X., H.K., G.K.L., T.S. and S.W. Visualization: Zhi Zhang, Zhenwen Zhang, B.J., Y.Y., Q.X. and X.Y. Funding acquisition: S.W. Supervision: S.W. Writing—original draft: S.W., Zhi Zhang, Zhenwen Zhang, B.J. and Y.Y. Writing—review and editing: Zhi Zhang, Zhenwen Zhang, B.J., Y.Y., T.S. and S.W.

Competing interests
The authors declare no competing interests.

Additional information
Extended data is available for this paper at https://doi.org/10.1038/s41567-026-03255-x.

Supplementary information The online version contains supplementary material available at https://doi.org/10.1038/s41567-026-03255-x.

Correspondence and requests for materials should be addressed to Gang Kevin Li, Thomas Schutzius or Steven Wang.

Peer review information *Nature Physics* thanks Edward Bormashenko, Gaurav Tomar and the other, anonymous, reviewer(s) for their contribution to the peer review of this work.

https://doi.org/10.1038/s41567-026-03255-x

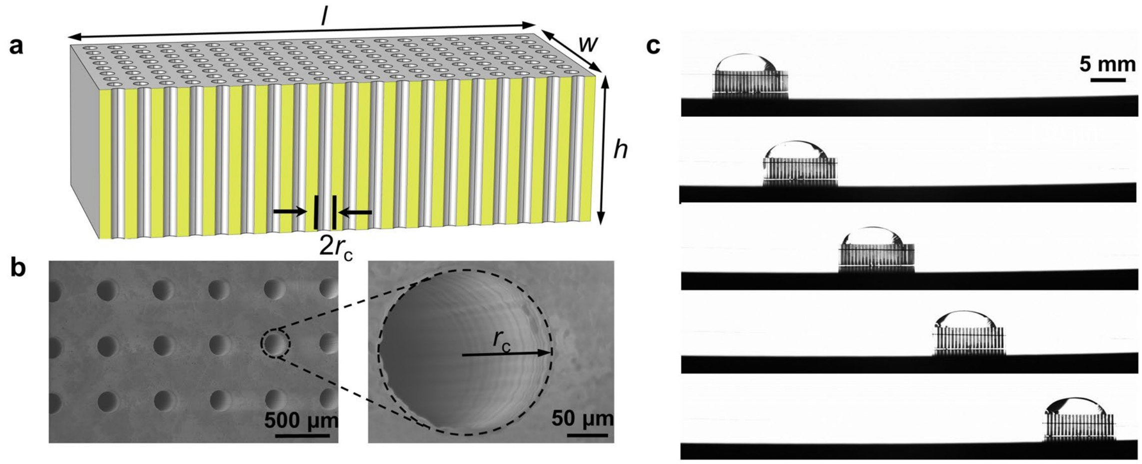

Extended Data Fig. 1 | CS structure and its Leidenfrost frictionless motion demonstrations. a, 3D structure of CS. **b**, scanning electron microscopy of capillaries. **c**, A sequence of high-speed images showing CS self-propulsion initiated by a droplet of 80 µL. The substrate is prescribed with a tiny angle of 0.5° to ensure unidirectional motion, and copper wires are employed to restrain CS within the focal length

 https://doi.org/10.1038/s41567-026-03255-x

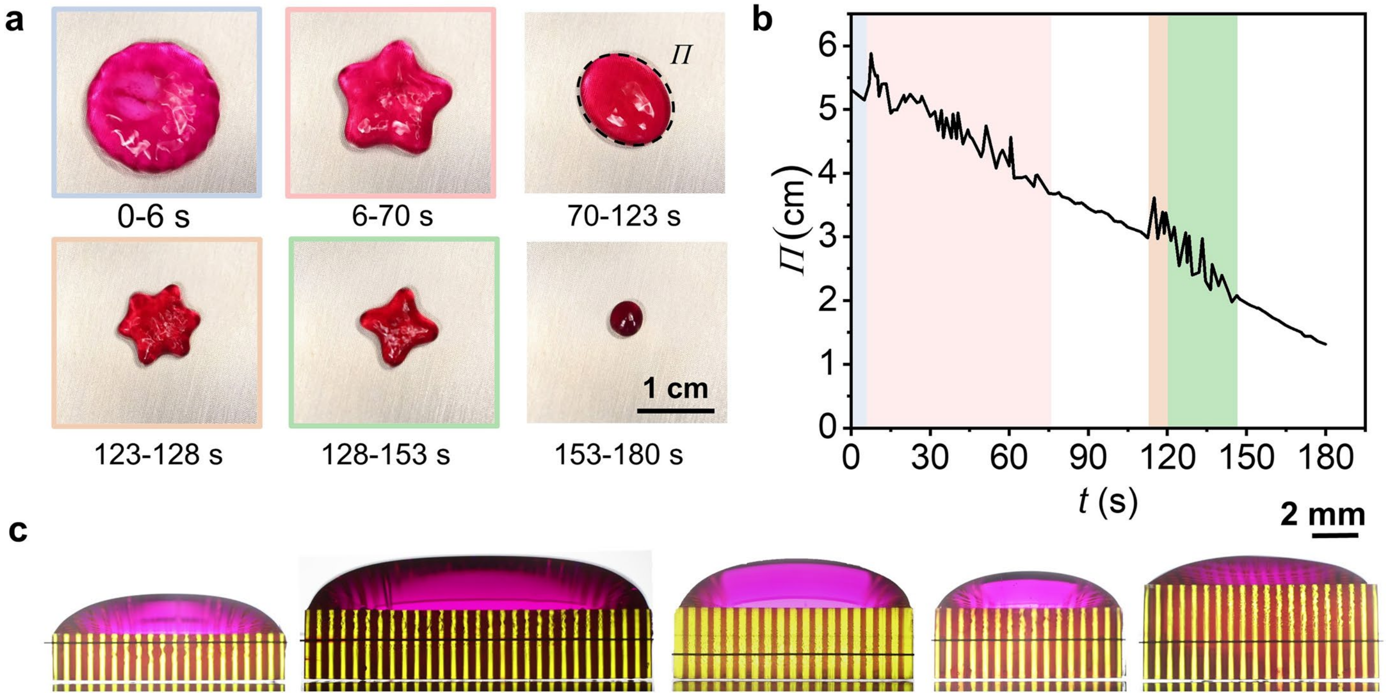

Extended Data Fig. 2 | Comparison between unstable Leidenfrost droplet oscillation and stable CS levitation state. a, Different droplet shape oscillations through its lifespan. **b**, Evolution of droplet equatorial perimeter (*Π*) with time. The color backgrounds highlight the corresponding star-shaped oscillations in Extended Data Fig. 2a. **c**, Robust Leidenfrost state of CSs across different dimensions.

https://doi.org/10.1038/s41567-026-03255-x

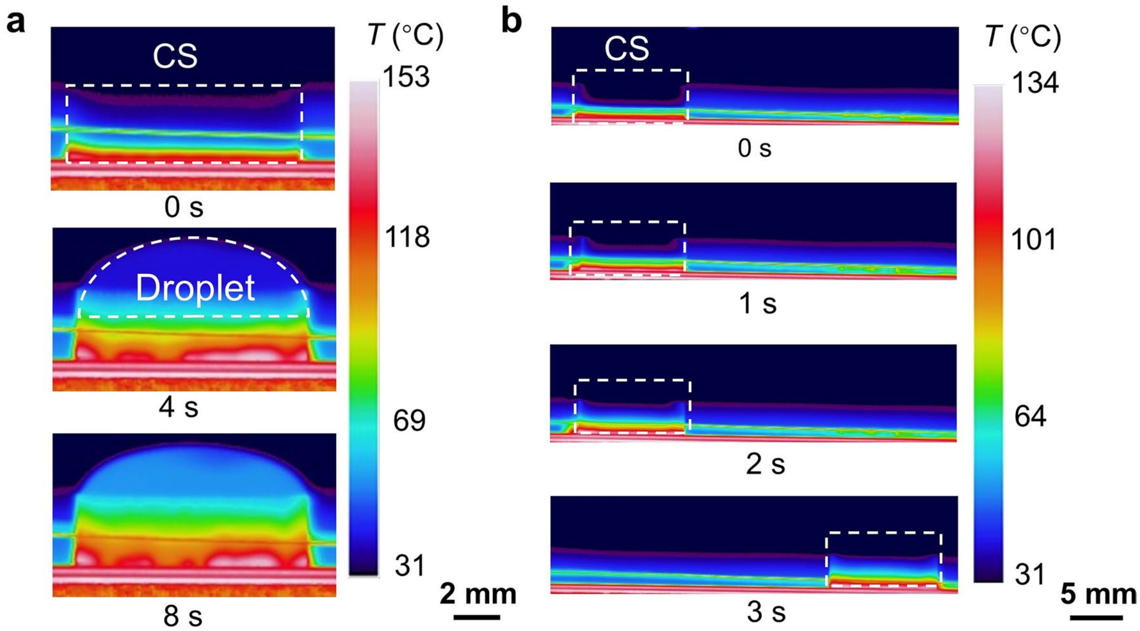

Extended Data Fig. 3 | Capillary Leidenfrost effect captured by an infrared high-speed camera. a, CS heating up process on a hot surface of 130 °C. **b**, Leidenfrost self-propulsion of CS on a substrate of only 110 °C, indicating the generation of lucubration vapor film beneath it. The droplet above is still not heated up before the start of self-propulsion, hence not visible in the infrared view.

https://doi.org/10.1038/s41567-026-03255-x

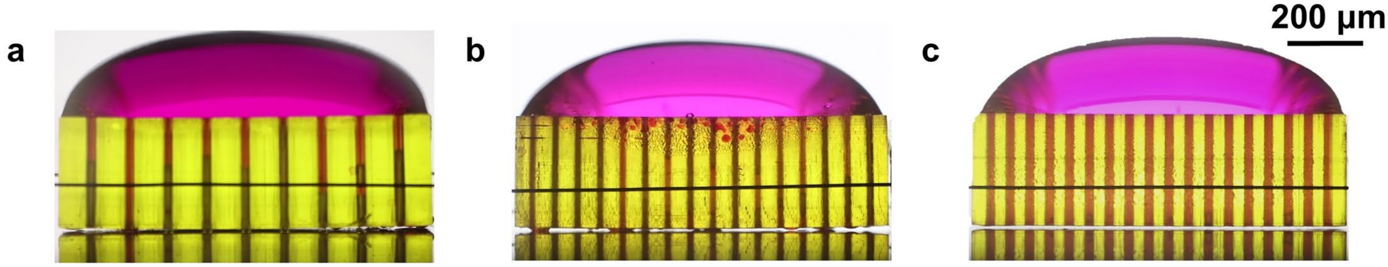

Extended Data Fig. 4 | Three distinct CS states at various capillary radii and porosities. a, Contact state, where CS cannot be levitated due to the low porosity. **b**, Mixed state, characterized by intermittent contact and oscillations. **c**, Levitation state, where a vivid vapor film is observed.

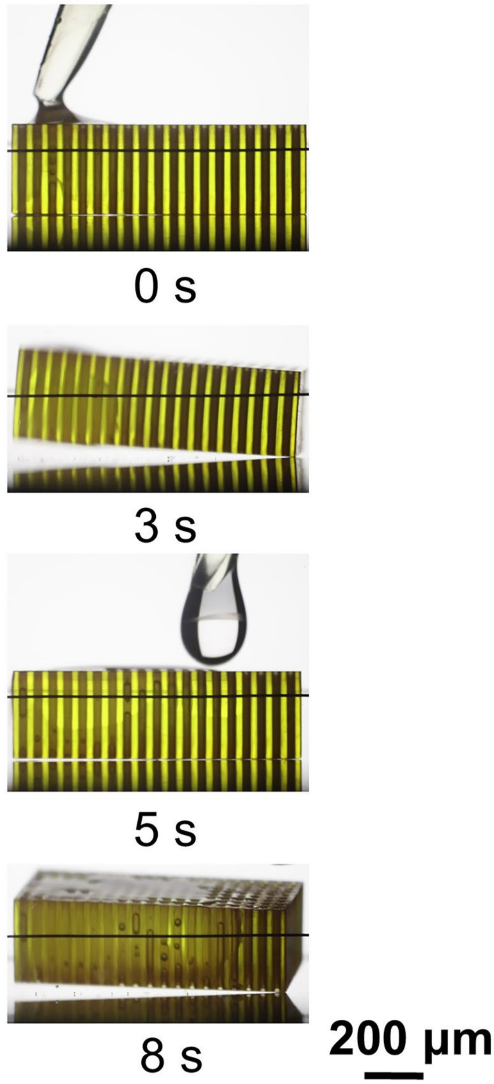

Extended Data Fig. 5 | Capillary Leidenfrost effect with ethanol. A sequence of images capturing the response of CS to ethanol drop impacts.

https://doi.org/10.1038/s41567-026-03255-x

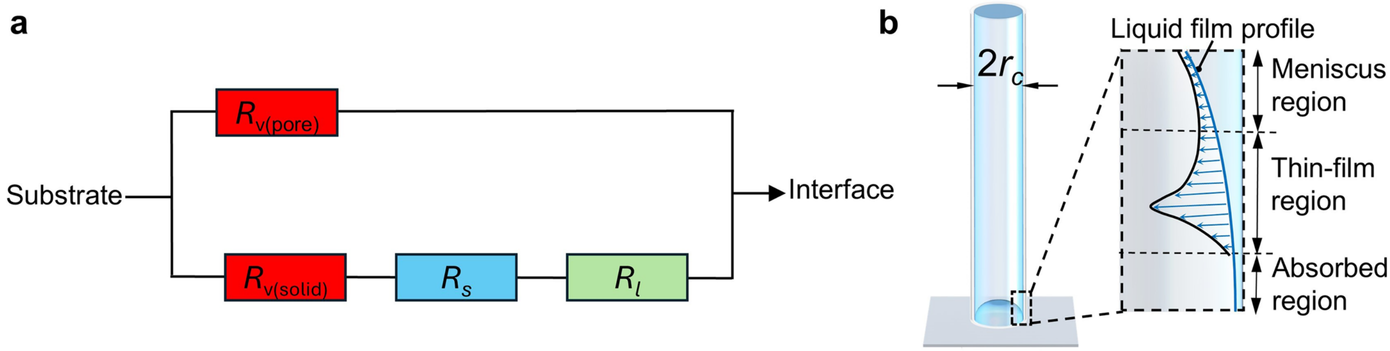

Extended Data Fig. 6 | Schematics for heat transfer process. a, Map of the dominant thermal resistance, identifying the two key paths governing the heat transfer process. **b**, Schematic for heat transfer at the meniscus. The meniscus is divided into three regions. The absorbed region (several nanometers), where evaporation is prevented by the strong adhesive force between liquid and capillary wall; The thin-film region (typically 10 -100 nm), where evaporation is remarkably enhanced and disjoining pressure is dominated; The meniscus region, where adhesive force is neglected, and capillary pressure is dominated. Evaporation primarily occurs in the thin-film region and meniscus region, and the blue arrow's length represents the evaporation flux distribution per length along the liquid film profile. The heat resistance of the liquid film is negligible compared with the heat resistance of the liquid film and the solid.

https://doi.org/10.1038/s41567-026-03255-x

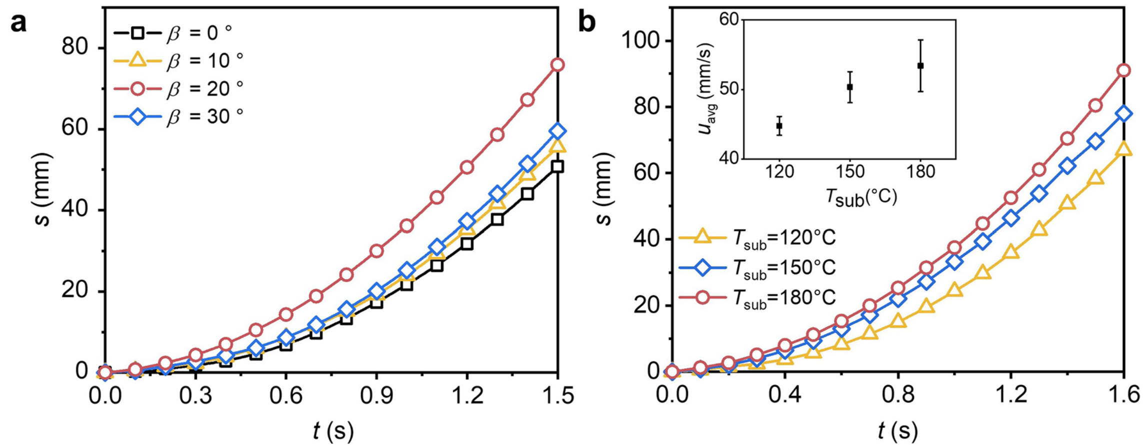

Extended Data Fig. 7 | Effect of capillary tilted angle and substrate temperature on CS self-propulsion. **a**, Travel distances of CS with varying β. **b**, Travel distances and average speeds of CS at distinct substrate temperatures. The testing samples number n = **3**, data are presented as mean values ± s.e.m.

Extended Data Fig. 8 | Novel CS design attempts. a, Self-propulsion of a racing car prototype with tilted capillaries design on a horizontal track. The time interval between two consecutive frames is 1 second. **b**, Frictionless motion of metallic CS. The time interval between two consecutive frames is 0.5 seconds, and the T_{sub} is 280 °C.

https://doi.org/10.1038/s41567-026-03255-x

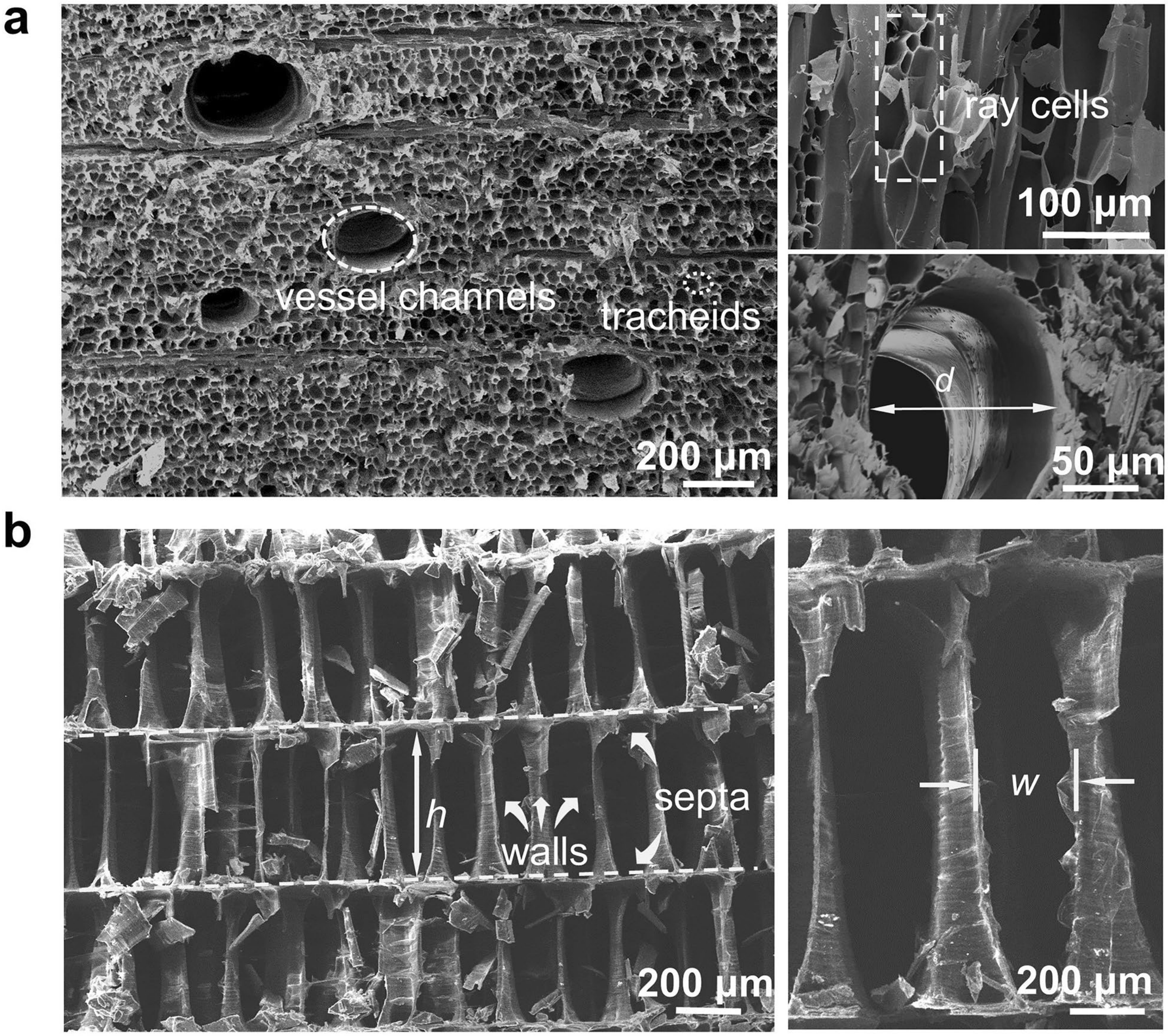

Extended Data Fig. 9 | Scanning electron microscopy images. a, Balsa wood. **b**, Cuttlebone.

 https://doi.org/10.1038/s41567-026-03255-x

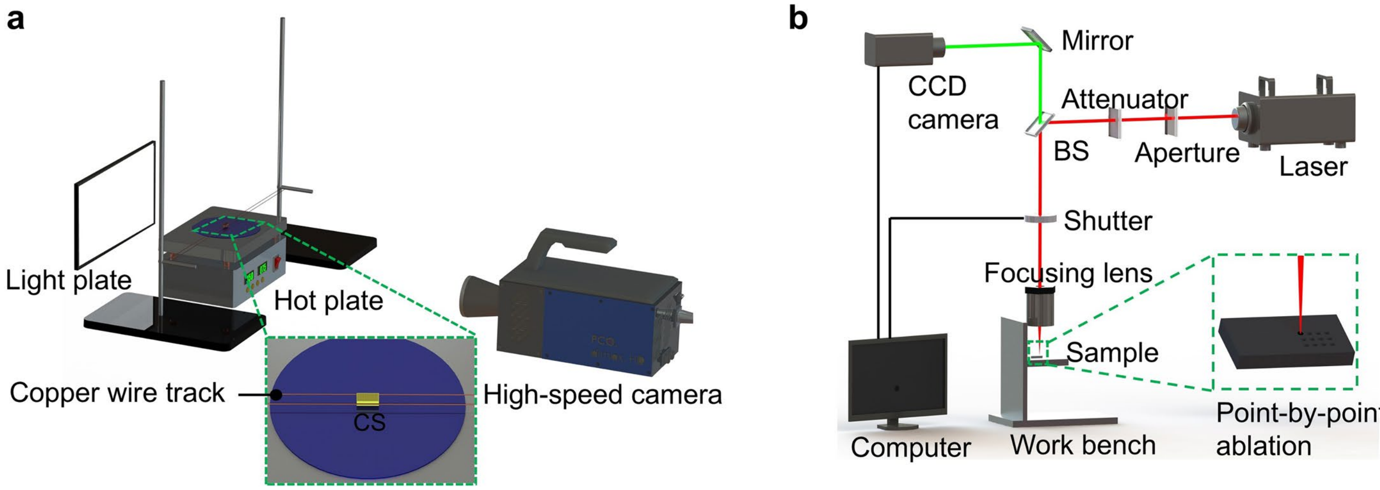

Extended Data Fig. 10 | Experimental setup schematics. a, High-speed camera imaging. **b**, Femtosecond laser processing.